Renewable Energy 91 (2016) 524–530

Contents lists available at ScienceDirect

Renewable Energy

journal homepage: www.elsevier.com/locate/renene

On the near-wall effects induced by an axial-flow rotor

N.J. Möller [a], H. Kim [b], V.S. Neary [c], M.H. García [a], L.P. Chamorro [a, b, *]

[a] Department of Civil and Environmental Engineering, University of Illinois, Urbana, IL 61801, USA
[b] Department of Mechanical Science and Engineering, University of Illinois, Urbana, IL 61801, USA
[c] Sandia National Laboratory, Albuquerque, NM 87123, USA

ARTICLE INFO

Article history:
Received 28 May 2015
Received in revised form
24 December 2015
Accepted 16 January 2016
Available online 11 February 2016

Keywords:
Bed shear stress
Channel flow
Hydrokinetic energy
Axial-flow turbines

ABSTRACT

Laboratory experiments were performed to quantify the near-wall flow characteristics and the bed shear stress in the vicinity of an axial-flow rotor model. It was placed in a smooth-wall open channel flow under subcritical conditions and operated at two heights. A laser Doppler velocimeter was used to collect profiles of the streamwise and vertical velocity at few locations within the rotor symmetry plane as close as one wall unit from the bed. Local estimates of the mean bed shear stress were obtained from the mean velocity profiles in the viscous and logarithmic regions. Results show that the bed shear stress is sensitive to the distance from the rotor and to the relative height of the rotor. Maximum bed shear stress occurred downstream of the rotor with the rotor closer to the bed. Flow statistics shows a reduction of turbulence intensity and turbulent shear stress near the wall and close to the rotor due to flow acceleration and changes in the pressure distribution. Spectral analysis of the streamwise velocity evidences a reduction of the energy content across scales spanning two decades right below the turbine. The increase of bed shear is due to mainly flow accelerating but not to turbulence.

1. Introduction

Marine and hydrokinetic (MHK) energy conversion has the potential to complement the renewable energy portfolio. MHK concepts are targeted to be deployed in various waterways such as streams, rivers, and tidal currents [8,13,16,25,38]. Recent estimates place the technically recoverable resource at 250 TWh/year for tidal, 163 TWh/year for ocean currents [just from Florida to North Carolina], and 120 TWh/year for undammed rivers [18,20]. Compared with standard hydropower sources, these concepts are weakly intrusive, leading to reduced effects on the nearby environment and ecosystem [21].

Quantitative characterization of the induced turbulence, its structure and diffusion features, rotor-induced bed shear stress, and its complex interaction with the ambient environment are still subjects of intensive research, not only to achieve optimal MHK turbine operation, but to determine potential environmental impacts and mitigation strategies associated with the relatively emergent technologies [3,24,39]. Axial-flow turbines can heavily modify the local structure of the flow by generating small-scale turbulence and dampening large-scale motions [4]. Velocity deficit due to energy conversion from the mean flow can persist far downstream with the wake expansion strongly constrained by the flow bed [29]. Rotor wakes are modulated by the dynamics of blade-tip and hub vortices [11] and exhibit complex meandering features in the far-wake region [5,23] that appear to be independent of the turbine operation [36].

Onset and dynamics of sediment motions due to increased shear from MHK generators are areas of particular interest due to their effects on water quality, and ecosystem health, among others [21]. Using a 1D morphological model and tidal data of the Bristol Channel in England [32], predicted a bed shear stress increase and scour in the region surrounding MHK turbines. Coherent turbulence structures can exert instantaneous drag and lift on the flow bed [6,7,15,34,35] and numerical simulations by Ref. [22] have shown that the generated turbulence and wake flow can modify the bed shear, which is key for triggering the onset of sediment motion in natural bedforms [14]. However, Reynolds-averaged boundary shear stresses cannot competently explain the sediment particle movements in the turbulent boundary layer, such as entrainment and transport [6,7], while high-fidelity turbulence measurement in wakes still lacks [5,30,31]. Further, numerical simulations have shown that turbine arrays have potential impact on the environment, including erosion streams alongside the turbine arrays with

* Corresponding author. Department of Mechanical Science and Engineering, University of Illinois, Urbana, IL 61801, USA.
E-mail address: lpchamo@illinois.edu (L.P. Chamorro).

http://dx.doi.org/10.1016/j.renene.2016.01.051
0960-1481/

deposition in the upstream [1], while array configuration with a spacing of five rotor diameters have been proposed to limit excessive hydrodynamic impacts from the MHK turbines [10].

Due to the recognized potential impact of the hydrokinetic turbines on the stability of natural beds, our fundamental study aims to offer insights on the flow structure in the vicinity of bed around a rotor model. Uncovering the flow physics in these situations can provide guidelines toward the general problem of placing hydrokinetic turbines without compromising the natural dynamics of the beds, which is key for the ecosystem and the targeted performance of turbine arrays. For this reason, unique and challenging experiments are designed and performed to characterize the flow features near a fix, smooth bed as close as the viscous sublayer around two rotor setups. To accomplish this, a high-resolution 2-component laser Doppler velocimetry (LDV) was used to obtain flow measurements. The LDV system allows for non-intrusive measurements [28] well within the viscous sublayer [33]. The experimental design and measurement procedure are described in Section 2. A quantitative characterization of the flow in the near-wall around the turbine is presented in Section 3 and the main conclusions are discussed in Section 4.

2. Experimental set-up

A three-blade axial-flow type rotor model was placed and operated in a smooth-wall open channel flow under subcritical conditions. The rotor has a diameter $d_T = 0.12$ m and its geometry mimics the reference model from Sandia National Laboratory. The cross section of the blades are part of the MHKF1 family of hydrofoils (MHKF1-180s, MHKF1-240s, and MHKF1-400), which is specifically designed for MHK power applications [40]. Fig. 1 illustrates a general schematic of the flume and the rotor and the relative location of the rotor within the flume. The turbine blades and nacelle were fabricated with PolyJet Vero photopolymers and 3D printed with an Objet Eden 350 machine with resolution of 50 μm. Table 1 summarizes the basic geometry of the turbine blades, which includes the chord length c, and pitch angle α as a function of the radial distance r. The turbine uses Precision Microdrives 112-001 Micro Core 12 mm DC Motor that serves a loading system. Instantaneous voltage from the DC generator was captured at 5 kHz with a Measurement Computing USB-1608HS DAQ, whose internal resistance provided the turbine power output.

The experiments were carried out in the Woods Hole Oceanographic Institute (WHOI) flume at the Ven Te Chow Hydrosystems Laboratory, University of Illinois. The flume is 17 m long, 0.6 m wide, 0.3 m deep, and able to adjust the longitudinal slope. The turbine was placed 13.7 m downstream from the inlet at the center of the flume cross section and under a $H = 0.25$ m water depth, providing a blockage ratio ~0.08, and a bulk flow velocity $U \approx 0.28$ ms^{-1}, which practically coincided with the velocity at the turbine hub U_{hub}. The turbine is installed upside down mimicking some of the existing structure designs [27] and rotor hub heights z_{hub} were set at $z_{hub}/d_T = 1.04$ (case a) and 0.65 (case b), giving submergences $S = (H - z_{hub})/d_T = 1.29$ and 1.68. The resulting Froude number is $Fr = U/(gH)^{1/2} = 0.18$, where g is the gravity acceleration, and the Reynolds numbers, based on the rotor diameter and the middle-span blade chord length (c_m), are $Re = U_{hub}d_T/\nu \sim 3.1 \times 10^4$ and $Re = U_{hub}c_m/\nu \sim 4 \times 10^3$, where ν is the kinematic viscosity. A sharp-crested weir located at the downstream end of the flume controlled the subcritical flow condition. A turbulent boundary layer of $\delta \approx 0.2$ m thickness and friction velocity $u_{*0} \approx 0.0118$ m s^{-1} characterized the incoming flow at ~ 4 rotor diameters upstream of the rotor. The turbine operated at constant tip-speed ratio $\lambda = \pi f_T d_T/U_{hub} \approx 4.0$, where f_T is the turbine frequency in Hz obtained from video recording and from the power output spectrum shown in Fig. 3, which resulted $f_T = 3$ Hz. The spectral distribution of the power output reveals that the rotor is insensitive to turbulence motions of reduced frequency $fd_T/U_{hub} \geq 1.2$ or, invoking Taylor's hypothesis, to length scales $l \leq 1.2d_T \sim O(d_T)$. This behavior is consistent with experiments of [5] with a larger rotor placed in a open channel flow.

Laser Doppler velocimetry (LDV) was used to obtain high-resolution and synchronous measurements of the streamwise (u) and vertical (w) velocity components of the flow. The LDV system includes a Spectra-Physics Stabilite 2017 Ar-Ion laser, TSI TR 60 Series (3-D, non-submersible) probe, TSI Model TLN06-363 (363 mm focal distance) lens, TSI Fiberlight Multi-Color Beam Generator 3-Component optical splitter, TSI PDM1000 photo detector module, TSI FSA3500/4000 signal processor, Tektronix oscilloscope, and TSI FlowSizer software. Flow velocity was

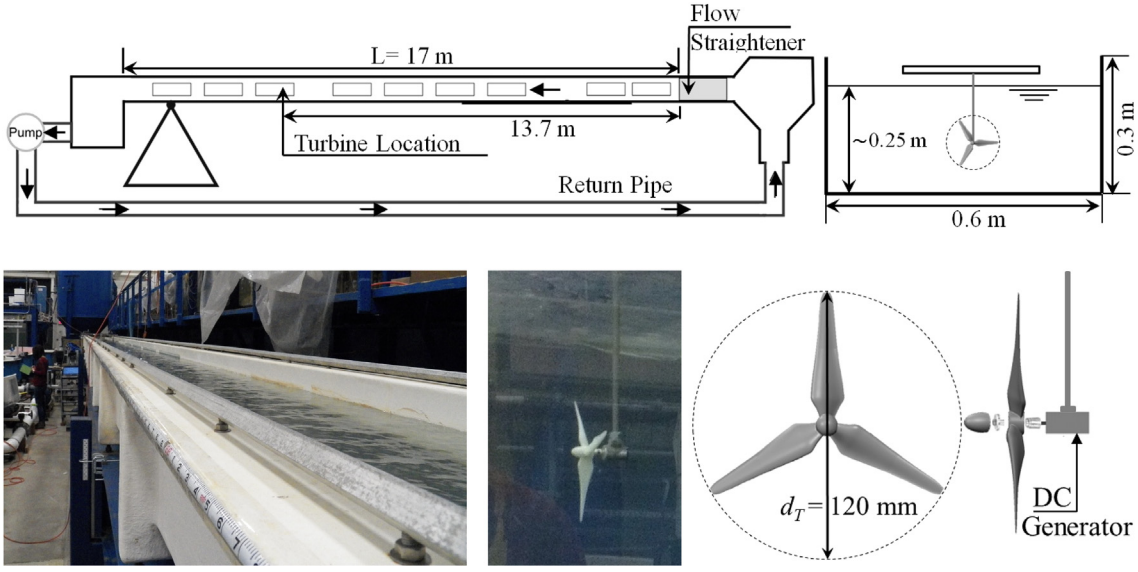

Fig. 1. Schematic of the flume and rotor location (top); and photographs of the flume and schematic the rotor (bottom).

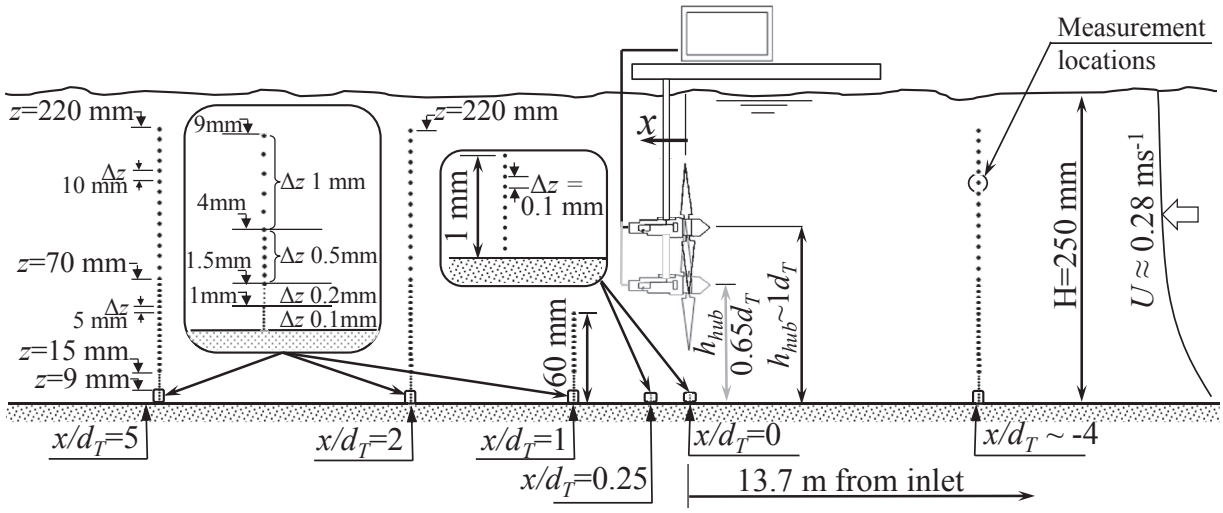

Fig. 2. General schematic around the rotor and measurement locations.

Table 1
Basic geometry of the turbine blades normalized by the rotor radius R: r is the radial distance, c is the chord length, and α is the (pitch) angle with respect to the rotor plane.

r/R	0.20	0.30	0.40	0.50	0.60	0.70	0.80	0.90	0.95
c/R	0.275	0.248	0.215	0.181	0.156	0.136	0.119	0.100	0.088
α (deg.)	31.8	23.9	17.7	12.8	9.4	7.5	6.0	4.6	3.9

obtained at few locations along the symmetry plane of the rotor where emphasis is placed on the very near-wall region (viscous sublayer). Selected vertical profiles of varied spacing ranging from $\Delta z = 0.1$ mm to 10 mm and heights (1 mm–200 mm) were taken at x/d_T~–4 (incoming flow), 0 (below the rotor), 0.25, 0.5, 2 and 5. Specific details of the measurement locations are illustrated in Fig. 2. Frequency sampling varied across the vertical locations due to reduced flow rate in the near wall region, and ranged from $f = 5$ Hz in the viscous sublayer to 50 Hz in the logarithmic and outer layers. To allow representative flow statistics, time sampling varied from 600 s (in the very near wall region) to 240 s in the outer flow.

3. Results and discussion

In this section, we present the flow statistics at the locations illustrated in Fig. 2 for the two rotor configurations defined in Section 2. Based on these measurements, we estimate the bed shear around the rotor.

3.1. Mean velocity profiles and bed shear stress

Mean velocity profiles in the viscous sublayer and log layer are used to estimate the mean bed shear stress around the turbine location. The velocity profiles are normalized with inner units i.e., $U^+ = f(z^+)$, where $U^+ = U/u_*$, $z^+ = u_* z/\nu$, $u_* = \sqrt{\tau_w/\rho}$ is the so-called friction velocity, τ_w is bed shear, ν is the kinematic viscosity and ρ is the fluid density. In the very near wall region within $z^+ \leq 5$, where the Reynolds stress is negligible, the velocity distribution over a hydrodynamically smooth wall is described by Equation (1):

$$U^+ = z^+. \tag{1}$$

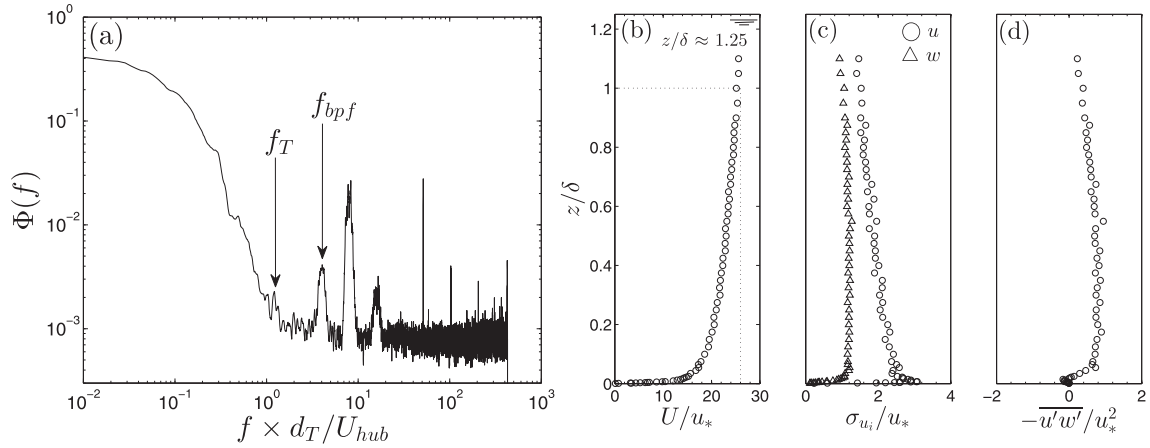

Fig. 3. (a) Spectrum of the power output fluctuations. f_T and f_{bpf} indicate turbine and blade-passing frequencies; characteristics of the incoming flow: (b) streamwise velocity U/u_*, (c) turbulence intensity σ_u/u_*, (d) Reynolds stress $-\overline{u'w'}/u_*^2$.

In canonical boundary layer flows, at z^+~30–300, the viscous effects are negligible and the shear stress is approximately constant. The velocity profile follows a log distribution characterized by:

$$U^+ = \frac{1}{\kappa} ln\left(z^+\right) + C^+, \quad (2)$$

where $\kappa \approx 0.41$ is the well-known Von Kármán constant and $C^+ \approx 5.2$ from experimental evidence [37]. The non-dimensional profiles of the incoming flow (x/d_T~−4), and right below the turbine ($x/d_T = 0$), as well as downstream of the turbine ($x/d_T = 0.25, 0.5, 1, 2$, and ~5) are shown in Fig. 4 for the rotor located at $z_{hub}/d_T = 1.04$ (case *a*) and at $z_{hub}/d_T = 0.65$ (case *b*). The velocity distributions from Equations (1) and (2) are included as a reference. The velocity profiles in both cases cover at least the viscous and log regions. However, the case *a* also includes velocity profiles of the incoming flow and turbine wake at $x/d_T = 2$ and 5 extending over the turbine top tip height to highlight the momentum deficit induced by the rotor and flow recovery with downstream distance [31]. Despite the flow behind the turbine is not adjusted, the profiles in both cases exhibit a self-similar behavior up to the log region, which allowed to estimate u_*. It is worth mentioning that the extension of the logarithmic regions is further constrained in the case *b* due to the proximity of the rotor to the wall and wake expansion. To highlight the collapse of the profiles in the viscous sublayer, Fig. 5 illustrates the velocity distribution for heights within $y^+ \leq 7$. The linear velocity distribution $U^+ = z^+$ is clearly observed up to z^+~5, with deviations occurring only over this height.

The estimates of the local bed shear stress obtained from the collapse of the velocity profiles are illustrated in Fig. 6 at various locations downstream of the model turbine for the two cases. The bed shear stress is normalized with that of the incoming flow and

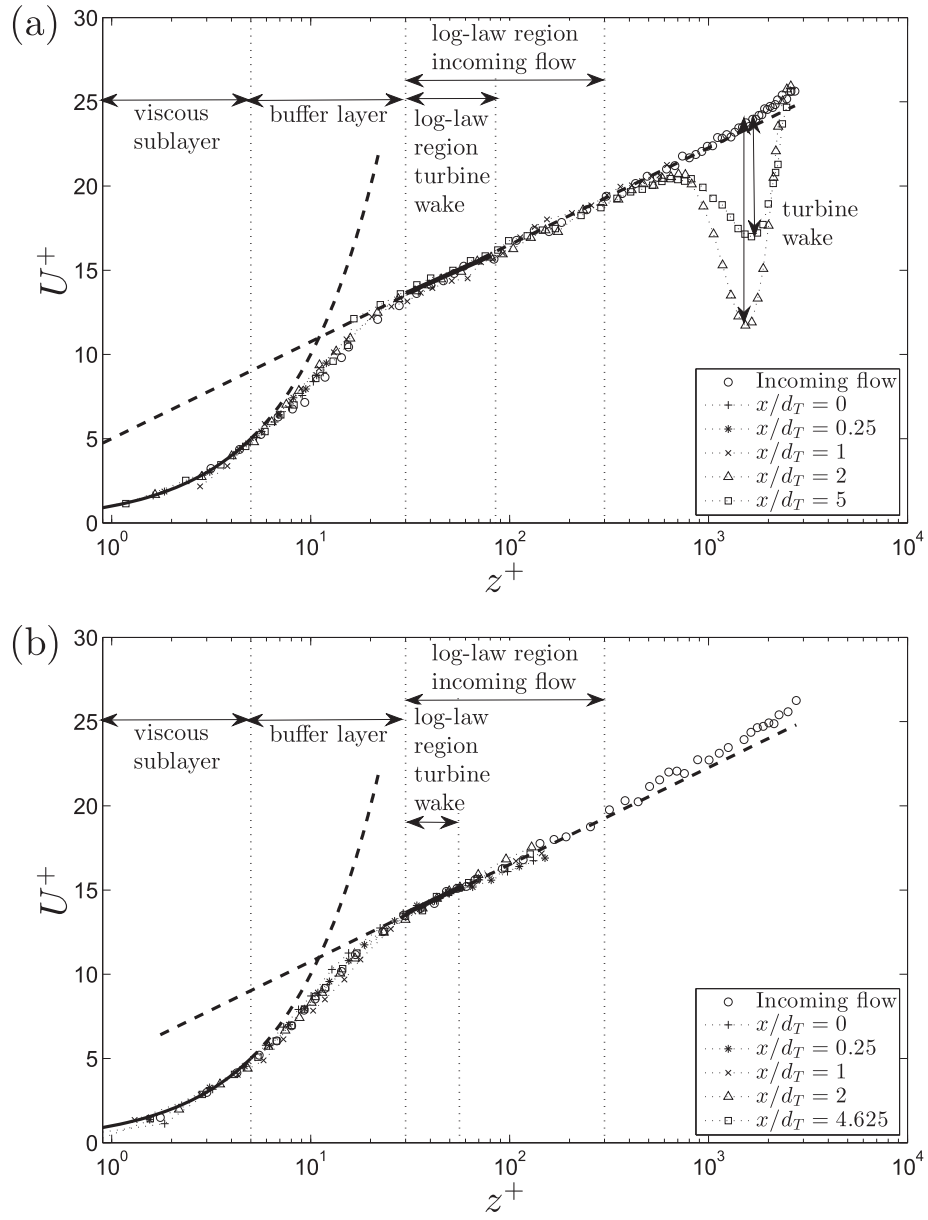

Fig. 4. Mean velocity profiles normalized with wall units for the turbine rotor located at (a) $z_{hub}/d_T = 1.04$; and (b) $z_{hub}/d_T = 0.65$. Theoretical distributions of the viscous sublayer and log layer are includes as a reference in dashed lines.

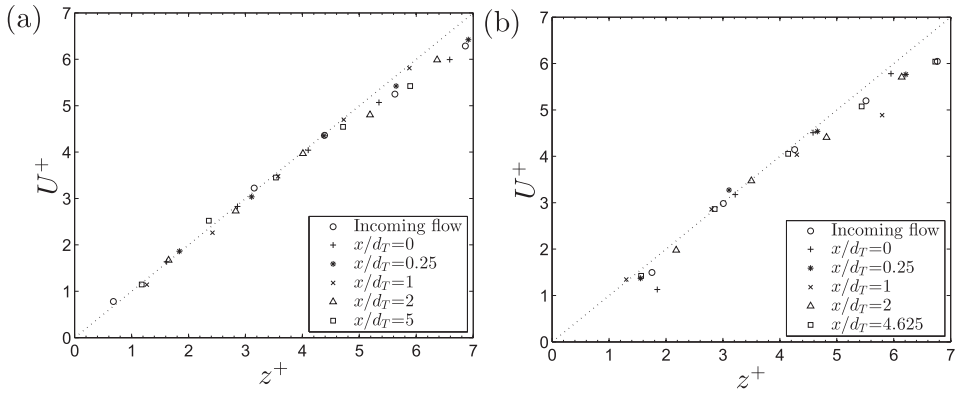

Fig. 5. Mean velocity profiles very near the wall normalized with wall units for the turbine rotor located at (a) $z_{hub}/d_T = 1.04$; and (b) $z_{hub}/d_T = 0.65$. Dotted line shows the $U^+ = z^+$ relationship of the viscous sublayer.

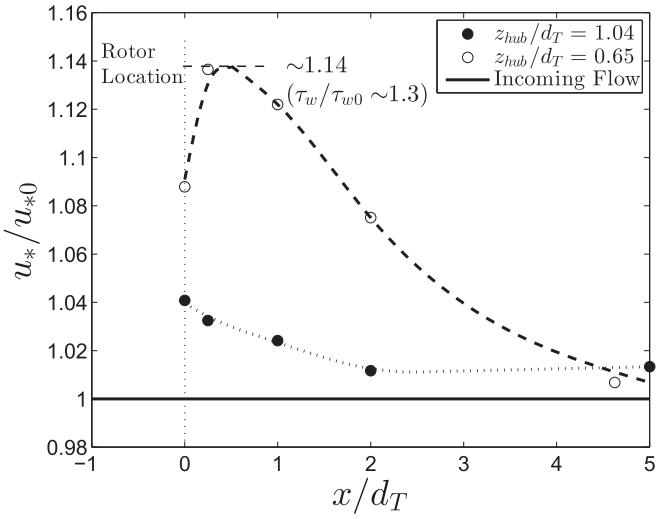

Fig. 6. Normalized friction velocity (u_*/u_{*0}) along the turbine axis at $z_{hub} = 1.04$ and $z_{hub} = 0.65$.

the distance with the rotor diameter. The figure shows a non-negligible effect of the relative rotor height z_{hub}/d_T on the magnitude and spatial distribution of u_*. Maximum u_*/u_{*0} reaches ~1.14 and ~1.04 (or increase of ~ 30% and ~ 8% on the bed shear stress) for the $z_{hub}/d_T = 1.04$ and $z_{hub}/d_T = 0.65$, while the changes of u_* extends up to x/d_T~5 and 2, respectively. The case with the rotor close to the wall ($z_{hub}/d_T = 0.65$) also shows that the maximum bed shear does not occur right below the rotor but at x/d_T~0.5. It probably happens only at the rotor central plane and is due to the flow acceleration outside the expanding wake. This downstream shift of the maximum u_* is not observed in the rotor located at $z_{hub}/d_T = 1.04$ probably due to the reduced flow acceleration. Overall, the $u_* = f(x/d_T, z_{hub}/d_T)$ relationship highlights the linkage between flow, wall and rotors and the potential onset of sediment motions when hydrokinetic turbines are placed over beds near critical equilibrium. In this case, bathymetry can change and substantially modify the momentum distribution in a river cross section, which can negatively impact the economy of a hydrokinetic project.

3.2. Turbulence statistics and turbine-induced spectral reorganization of the flow

Streamwise turbulence intensity σ_u/u_* and normalized Reynolds stress $-\overline{u'w'}/u_*^2$ are shown in Fig. 7 for the two cases. In the case *a* ($z_{hub}/d_T = 1.04$), the near-wall turbulence statistics in the vicinity of the rotor exhibit distributions similar to those of canonical flows, where maximum of turbulence levels occur around z^+~15 [9,26]. Within the rotor wake region, statistics resemble that of the case given by Ref. [5] on a similar but larger setup, with deviations at hub and tip vortices while showing no significant change otherwise [31]. The similarity features of these statistics appears, however, to

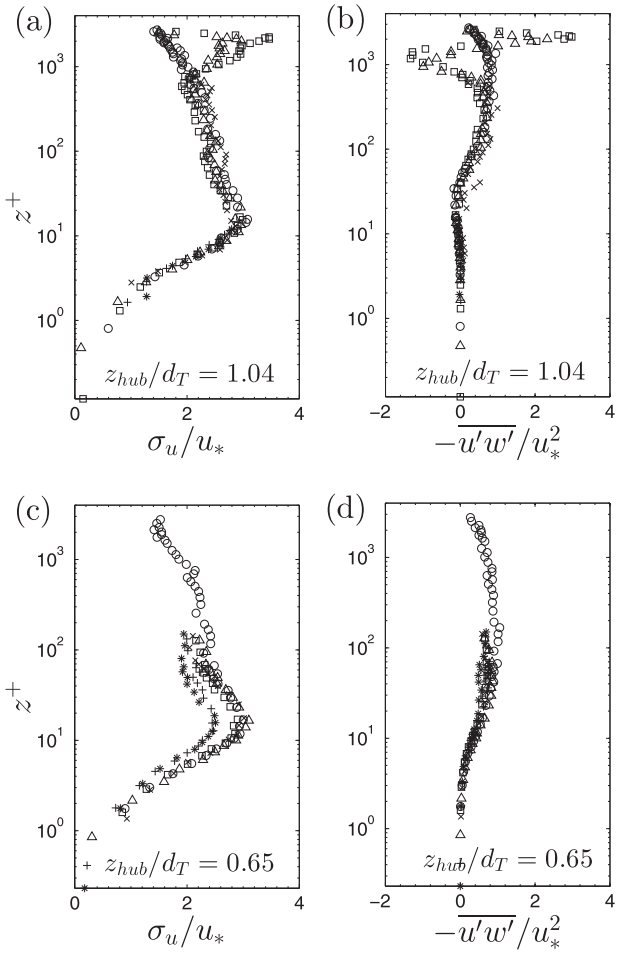

Fig. 7. Streamwise turbulence intensity σ_u/u_*. Symbols°, incoming flow; .+$x/d_T = 0$ *$x/d_T = 0.25$ × $x/d_T = 1$ △$x/d_T = 2$ □ $x/d_T = 5$.

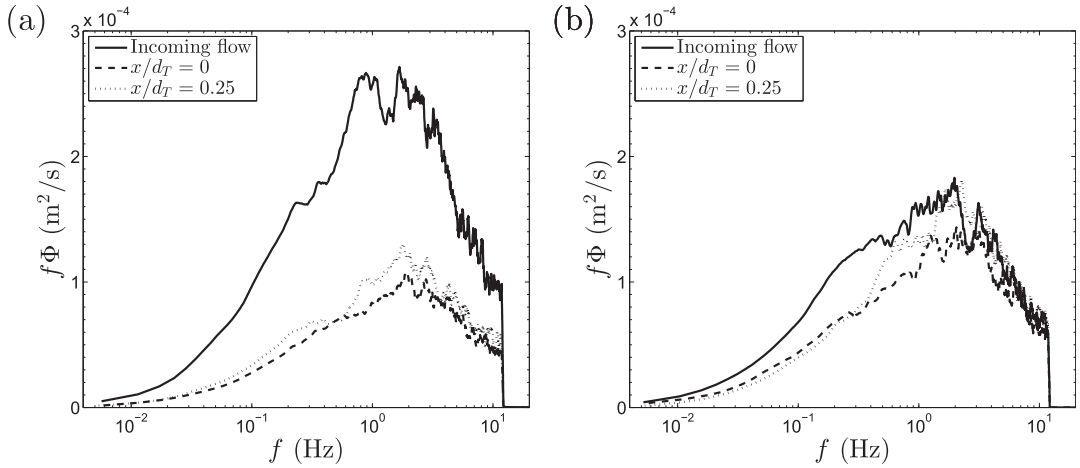

Fig. 8. Pre-multiplied power spectra ($f\Phi$) of the incoming flow, at $x/d_T = 0$, and at $x/d_T = 0.25$ with $z_{hub}/d_T = 0.65$ hub height setting: (a) $z^+ = 10$; and (b) $z^+ = 12$.

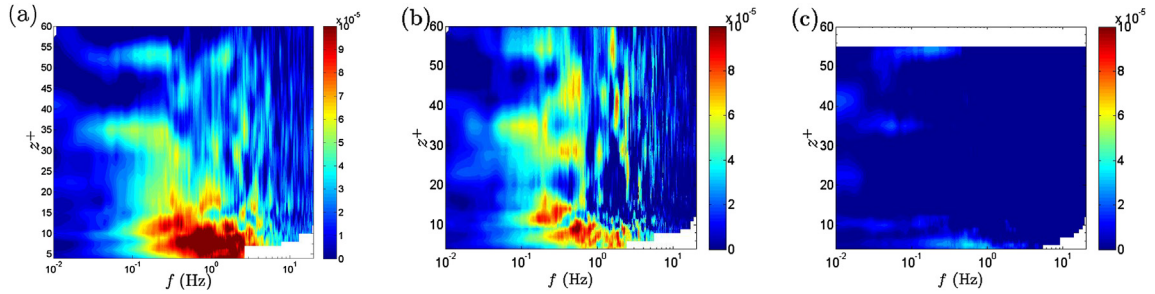

Fig. 9. 2D pre-multiplied spectral difference ($\Delta f\Phi_u$) between the incoming flow and that at (a) $x/d_T = 0$, (b) $x/d_T = 0.25$, and (c) $x/d_T = 2$. $z_{hub}/d_T = 0.65$ case.

break down in the case b ($z_{hub}/d_T = 0.65$) and close to the rotor at $x/d_T = 0$ and 0.25 (see Fig. 7c,d). It might be due to the local flow acceleration induced by the proximity of the rotor to the bed, leading to changes in the local pressure gradient and consequently departure from the similarity behavior [12].

The local reduction of the turbulence near the rotor in the case b can be further inspected by comparing the structural distribution of the turbulence with that of the incoming flow. Fig. 8 illustrates the pre-multiplied spectra, $f\Phi$, of the streamwise velocity of the incoming flow, included as a reference and wake at $x/d_T = 0$ and $x/d_T = 0.25$ at $z^+ = 10$ and $z^+ = 12$ for the case b. This figure shows that the energy content of the organized turbulence motions is dampened across all the scales resolved. In particular, the large-scale motions, populating the incoming flow and characterizing the near wall region turbulence [2,17,19], are dampened below the rotor bottom tip. To better illustrate these differences at various heights, 2D pre-multiplied spectral difference ($\Delta f\Phi_u$) between the incoming flow and $x/d_T = 0$, 0.25 and 2 (case b) near the wall ($z^+<60$) is shown in Fig. 9. It suggests that the spectral energy content is mostly dampened within heights below the buffer layer and contained within a frequency band extending roughly two decades. The energy content reduction is the highest right below the rotor, which appears to reduce rapidly with downstream distance to practically recover the features of the incoming flow at x/d_T~2. These results further suggests that the enhanced shear at the wall (14% increase in u_* or ~30% of τ_w) is mainly due to local flow acceleration, not to turbulence.

4. Conclusions

Detailed characterization of the flow velocity in the vicinity of a rotor model, including the viscous sublayer, allowed the estimation of the bed shear stress distribution and turbulence features at various locations along the axis of the rotor. Results show that the bed shear stress is very sensitive to the distance from the rotor and to the relative height of the rotor z_{hub}/d_T. Specifically, bed shear slightly changed with the rotor located at z_{hub}/d_T~1; however, an increase of 30% occurred with the rotor at $z_{hub}/d_T = 0.65$. Turbulence level is comparatively lower in regions of increased bed shear, suggesting that the likelihood of particulate notion in beds is due to flow acceleration. Comparison of the spectral content of the flow turbulence below the rotor and that of the incoming flow shows a damping of the turbulent energy across scales spanning two decades. It indicates that the flow/bed dynamics near hydrokinetic turbines is dominated by small-scale turbulence. This study provides insights for assessing potential erosion near the turbine based on local bed sediments and turbine proximity to bed. Subsequent work will consider near wall characterization of the flow under multiple rotor scenarios with various tip-speed ratios. To the best knowledge of authors, these type of measurements around rotating rotors have not been performed experimentally.

Acknowledgments

This work was supported by the Department of Mechanical Science and Engineering, University of Illinois at Urbana-Champaign, as part of the start-up package of Leonardo P. Chamorro. NJM was supported by the Chester and Helen Siess Professorship in Civil Engineering. The LDV system was obtained through a DURIP grant from the Office of Naval Research (N00014-06-1-0661) to Prof. Marcelo Garcia.

References

[1] R. Ahmadian, R.A. Falconer, Assessment of array shape of tidal stream turbines on hydro-environmental impacts and power output, Renew. Energy 44 (2012) 318–327.

[2] B. Balakumar, R. Adrian, Large scale and very large scale motions in turbulent boundary layers and channel flows, Phil. Trans. R. Soc. A 365 (2007) 665–681.

[3] G. Cada, J. Ahlgrimm, M.L. Bahleda, T. Bigford, S.D. Stavrakas, D. Hall, R. Moursund, M. Sale, Potential impacts of hydrokinetic and wave energy conversion technologies on aquatic environments, Fisheries 32 (2007) 174–181.

[4] L.P. Chamorro, M. Guala, R. Arndt, F. Sotiropoulos, On the evolution of turbulent scales in the wake of a wind turbine model, J. Turbul. 13 (27) (2012) 1–13.

[5] L.P. Chamorro, C. Hill, S. Morton, C. Ellis, R.E.A. Arndt, F. Sotiropoulos, On the interaction between a turbulent open channel flow and an axial-flow turbine, J. Fluid Mech. 716 (2013) 658–670.

[6] N.J. Clifford, J.R. French, J. Hardisty (Eds.), Turbulence: Perspectives on Flow and Sediment Transport, Wiley, 1993.

[7] P. Diplas, R. Kuhnle, J. Gray, D. Glysson, T. Edwards, Sediment Transport Measurements, chap. 5, American Society of Civil Engineers, 2008, pp. 307–353, http://dx.doi.org/10.1061/9780784408148.ch05.

[8] B. Drew, A.R. Plummer, M.N. Sahinkaya, A review of wave energy converter technology, Proc. Inst. Mech. Eng. A J. Power Energy 223 (2009) 887–902.

[9] P.A. Durbin, A reynolds stress model for near-wall turbulence, J. Fluid Mech. 249 (1993) 465–498.

[10] D. Fallon, M. Hartnett, A. Olbert, S. Nash, The effects of array configuration on the hydro-environmental impacts of tidal turbines, Renew. Energy 64 (2014) 10–25.

[11] M. Felli, R. Camussi, F. Di Felice, Mechanisms of evolution of the propeller wake in the transition and far fields, J. Fluid Mech. 682 (2011) 5–53.

[12] H.H. Fernholz, D. Warnack, The effects of a favourable pressure gradient and of the reynolds number on an incompressible axisymmetric turbulent boundary layer. Part 1. The turbulent boundary layer, J. Fluid Mech. 359 (1998) 329–356.

[13] P.L. Fraenkel, Power from marine currents, Proc. Inst. Mech. Eng. A J. Power Energy 216 (2002) 1–14.

[14] M.H. García, Sediment transport and morphodynamics, Sediment. Eng. (2008), http://dx.doi.org/10.1061/9780784408148.ch02, 21–163.

[15] M.H. García, F. López, Y. Niño, Characterization of near-bed coherent structures in turbulent open channel flow using synchronized high-speed video and hot-film measurements, Exp. Fluids 19 (1) (1995) 16–28.

[16] A. Gorlov, Tidal energy, in: J.H. Steele (Ed.), Encyclopedia of Ocean Sciences, Academic Press, Oxford, 2001, pp. 2955–2960.

[17] M. Guala, M. Metzger, B. McKeon, Scale interaction in the high reynolds number turbulent boundary layer, J. Fluid Mech. 666 (2011) 573–604.

[18] K.A. Haas, Assessment of Energy Production Potential from Tidal Streams in the United States, Technical Report, Georgia Tech Research Corporation, 2011.

[19] N. Hutchins, I. Marusic, Evidence of very long meandering features in the logarithmic region of turbulent boundary layers, J. Fluid Mech. 579 (2007) 1–28.

[20] P.T. Jacobson, T.M. Ravens, K.W. Cunningham, G. Scott, Assessment and Mapping of the Riverine Hydrokinetic Resource in the Continental United States, Technical Report, Electric Power Research Institute, 2012.

[21] S. James, E. Seetho, C. Jones, J. Roberts, Simulating Environmental Changes Due to Marine Hydrokinetic Energy Installations, in Oceans, 20-23 Sept Seattle, WA, 2010, pp. 1–10, http://dx.doi.org/10.1109/OCEANS.2010.5663854.

[22] S. Kang, I. Borazjani, J. Colby, F. Sotiropoulos, Numerical simulation of 3d flow past a real-life marine hydrokinetic turbine, Adv. Water Res. 39 (2012) 33–43.

[23] S. Kang, X. Yang, F. Sotiropoulos, On the onset of wake meandering for an axial flow turbine in a turbulent open channel flow, J. Fluid Mech. 744 (2014) 376–403.

[24] M. Khan, G. Bhuyan, A. Moshref, K. Morison, An Assessment of Variable Characteristics of the Pacific Northwest Regions Wave and Tidal Current Power Resources, and Their Interaction with Electricity Demand & Implications for Large Scale Development Scenarios for the Region, Tech. Repp. 17485–21-00 (Rep 3), 2008.

[25] M. Khan, M. Iqbal, J. Quaicoe, River current energy conversion systems: progress, prospects and challenges, Renew. Sust. Energy Rev. 12 (2008b) 2177–2193.

[26] J. Kim, P. Moin, R. Moser, Turbulence statistics in fully developed channel flow at low reynolds number, J. Fluid Mech. 177 (1987) 133–166.

[27] L. Lago, F. Ponta, L. Chen, Advances and trends in hydrokinetic turbine systems, Energy Sust. Dev. 14 (2010) 287–296.

[28] J.M. Mier, M.H. Garcia, Erosion of glacial till from the st. clair river (great lakes basin), J. Gt. Lakes. Res. 37 (2011) 399–410.

[29] L. Myers, A. Bajah, R. Rawlinson-Smith, M. Thomson, The effect of boundary proximity upon the wake structure of horizontal axis marine current turbines, in: Proceedings of the ASME 27th Conference, 2008. OMAE2008–57667. Portugal.

[30] L.E. Myers, A.S. Bahaj, Experimental analysis of the flow field around horizontal axis tidal turbines by use of scale mesh disk rotor simulators, Ocean. Eng. 37 (2010) 218–227.

[31] V.S. Neary, B. Gunawan, C. Hill, L.P. Chamorro, Near and far field flow disturbances induced by model hydrokinetic turbine: ADV and ADP comparison, Renew. Energ 60 (2013) 1–6.

[32] S.P. Neill, E.J. Litt, S.J. Couch, A.G. Davies, The impact of tidal stream turbines on large-scale sediment dynamics, Renew. Energy 34 (2009) 2803–2812.

[33] I. Nezu, A. Kadota, H. Nakagawa, Turbulent structure in unsteady depth-varying open-channel flows, J. Hydraul. Eng. 123 (9) (1997) 752–763.

[34] Y. Niño, M.H. García, Experiments on particleturbulence interactions in the nearwall region of an open channel flow: implications for sediment transport, J. Fluid Mech. 326 (1996) 285–319.

[35] Y. Niño, F. Lopez, M.H. Garcia, Threshold for particle entrainment into suspension, Sedimentology 50 (2003) 247–263.

[36] V.L. Okulov, I.V. Naumov, R.F. Mikkelsen, I.K. Kabardin, J.N. Srensen, A regular strouhal number for large-scale instability in the far wake of a rotor, J. Fluid Mech. 747 (2014) 369–380.

[37] S. Pope, Turbulent Flows, Cambridge University Press, UK, 2000, p. 771.

[38] F.O. Rourke, F. Boyle, A. Reynolds, Marine current energy devices: current status and possible future applications in ireland, Renew. Sust. Energy Rev. 14 (2010) 1026–1036.

[39] M.A. Shields, L.J. Dillon, D.K. Woolf, A.T. Ford, Strategic priorities for assessing ecological impacts of marine renewable energy devices in the pentland firth, Mar. Policy 33 (4) (2009) 635–642.

[40] H. Shiu, C.P. van Dam, E. Johnson, M. Barone, R. Phillips, W. Straka, A. Fontaine, M. J., A design of a hydrofoil family for current-driven marine-hydrokinetic turbines, in: Proceedings of the 20th International Conference on Nuclear Engineering and the ASME 2012 Power Conference, Anaheim, CA, 2009.